

Linear versus nonlinear modeling of black hole ringdownsYi Qiu^{1,2,3,4} Xisco Jiménez Forteza^{3,5,6,7,8} and Pierre Mourier^{8,3,5}¹*Department of Physics, The Pennsylvania State University, University Park Pennsylvania 16802, USA*²*School of Physics, Dalian University of Technology, Dalian 116024, China*³*Max Planck Institute for Gravitational Physics (Albert Einstein Institute), Callinstraße 38, 30167 Hannover, Germany*⁴*School of Astronomy and Space Science, Nanjing University, Nanjing 210023, China*⁵*Leibniz Universität Hannover, 30167 Hannover, Germany*⁶*Nikhef, Science Park 105, 1098 XG Amsterdam, The Netherlands*⁷*Institute for Gravitational and Subatomic Physics (GRASP), Utrecht University, Princetonplein 1, 3584 CC Utrecht, The Netherlands*⁸*Departament de Física, Universitat de les Illes Balears, IAC3-IEEC, E-07122 Palma, Spain*

(Received 11 January 2024; accepted 26 February 2024; published 26 March 2024)

The ringdown (RD) phase of gravitational waves is of prime interest for testing general relativity (GR). The modeling of the linear quasinormal modes (QNMs) within the Kerr spectrum—or with agnostic parametrized deviations to that GR spectrum—has become ordinary; however, specific attention has recently emerged to calibrate the effects of nonlinear perturbations for the predominant quadrupolar $l = 2$, $m = 2$ mode. In this paper, we test the performance of a few nonlinear toy models and of the nonlinear inspiral-merger-ringdown (IMR) model IMRPhenomD for faithfully representing the RD regime and we compare them with the results obtained using linear solutions as sums of QNM tones. Using several quasicircular, nonprecessing numerical waveforms, we fit the dominant $l = 2$, $m = 2$ mode of the strain, and we assess the results in terms of both the Bayes factor and the inferred posterior distributions for the mass and spin of the final black hole. We find that the nonlinear models can be comparable or preferred over the linear QNM-only solutions when the analysis is performed from the peak of the strain, especially at high signal-to-noise ratios consistent with third-generation observatories. Since the calibration of the tones' relative amplitudes and phases in high-overtone models to the progenitor parameters is still missing, or even not achievable, we consider the use of nonlinear models to be more pertinent for performing confident tests of general relativity based on the RD regime starting from early times.

DOI: [10.1103/PhysRevD.109.064075](https://doi.org/10.1103/PhysRevD.109.064075)**I. INTRODUCTION**

Gravitational waves (GWs) provide an excellent arena to study gravity on its strongest regime. Since the breakthrough observation of the first event GW150914 [1], the GW field itself has experienced an unprecedented growth, as a result of the early-on unexpected but nowadays confirmed high number of GW events observed. Currently, the number of confirmed GW events from compact binary mergers has risen significantly, summing up to about 90 in the last completed observing run (O3) [2–7] of the LIGO-Virgo-KAGRA (LVK) Collaboration [8–10]. While these

observations have already allowed us to set extraordinary constraints on the general theory of gravity (see, e.g., [11–14]), the near-future prospects are even more promising, with about 200 new events anticipated by the end of the current LVK O4 run [15]. The number of observed binary black hole (BBH) mergers is dominating the LVK event catalog. A typical BBH GW event is described by three different regimes; the inspiral, the merger, and the ringdown (RD). For the optimized search and characterization of the signals, the IMR gravitational waveform templates are used. IMR models are calibrated to numerical relativity (NR) solutions and provide us with the most accurate representation of the full waveform. For BBH mergers, current IMR waveform approximants are normally split into three different families: the IMRPhenom [16], SEOBNR [17], TEOB [18] and NRSurrogates (for a detailed description of the models see [19–22] and the references therein).

Published by the American Physical Society under the terms of the Creative Commons Attribution 4.0 International license. Further distribution of this work must maintain attribution to the author(s) and the published article's title, journal citation, and DOI. Open access publication funded by the Max Planck Society.

The study of the RD regime has drawn some attention in the last recent years. The RD describes the post-merger phase, in which the final, perturbed BH relaxes rapidly towards its stationary Kerr configuration, a phase which is associated with a characteristic late train of radiation [23–27]. Linear perturbation theory provides a simple description of this late radiation regime in the form of a countably infinite sum of damped sinusoids. Each damped sinusoid—or mode (lmn) —is at most described by four parameters, namely its frequency, damping time, amplitude and phase. The family of frequencies and damping times is known as the quasinormal-mode (QNM) spectrum [23–25] and, by virtue of the BH no-hair theorem, is uniquely determined by the final BH mass and spin [28–30]. The set of amplitudes and phases is determined by the progenitor parameters and the initial orbital conditions [31–37]. The BH no-hair theorem is tested through two common scenarios: namely, by performing an inspiral-merger-ringdown (IMR) consistency test [38] and through BH spectroscopy [39]. BH spectroscopy typically targets the independent estimation of the spectrum of at least two separate RD modes although GR deviations can be also measured with a single mode if one considers information from the progenitor BHs [13,14,40]. So far, several works from different groups dispute the successful/unsuccessful multiple-mode testing of the theorem with the loud-RD events GW150914 [13,41–50] and GW190521 [13,51–55]. In coming years, robust testing of the no-hair theorem [56] through BH spectroscopy may be achieved with loud events at LVK design sensitivity (see [57,58]) and become more precise at the LIGO A# sensitivity [59], reaching even the percent accuracy with third-generation gravitational wave interferometers such as the Einstein Telescope (ET) [60], Cosmic Explorer (CE) [61] and LISA [62], thanks to the expected and promising gain in signal-to-noise ratios (SNRs).

One of the major debates among the BH ringdown community pertains to the suitability of linear perturbation theory for describing the whole RD regime [41–43,45,63–69]. On the one hand, some previous works advocate that the results of linear perturbation theory can be applied from the peak of the gravitational strain onwards, which implies that the nonlinear effects observed at the merger regime become quickly irrelevant [66,70]. This is assessed by fitting to NR data the RD models with a large number of QNM tones—typically $N = 7$ overtones in addition to the fundamental mode—to obtain an accurate recovery of the BH parameters, while fixing its QNM spectrum to GR. On the other hand, such claims have been disputed by other works by observing that a high instability of high-overtone models can arise due to (i) a likely overfitting of the data and (ii) neglecting the yet unmodeled nonlinear contributions on the dominant $lm = 22$ mode [64,67,71,72]. In particular, even the linear-order contributions arising from the branch

cut,¹ such as the prompt response or the late tail effects [75–77], are neglected by ringdown models solely based on QNMs. Moreover, [68,78] have found clear evidences of quadratic contributions in higher harmonics of the RD (specifically, quadratic contributions to the $lm = 44$ mode sourced by the first-order 22-mode perturbations), which provide more accurate and more stable models than the linear models for these modes. Separately, similar conclusions are obtained by studying the shear at the horizon in head-on BH collisions [72,79]. Unfortunately, an analogous but conclusive analysis for the quadrupolar and dominant 22 mode in quasicircular mergers is still absent.

In this work we have tested the performance of linear and nonlinear RD models, by fitting the post-peak regime of NR waveforms from the SXS and the (associated) Ext-CCE NR catalogs [80]. The SXS NR waveforms are extracted at finite radii and then extrapolated to future null infinity. The Ext-CCE waveforms use the Cauchy characteristic extraction procedure, thus reducing significantly the gauge dependence of the waveforms obtained at null infinity. We consider the following RD models to fit the data: (i) and (ii) two RD models described by linear perturbation theory with a variable number of tones, with or without degrees of freedom allowing for restricted deviations from the GR QNM spectrum; (iii) the RD sector of the nonlinear IMRPhenomD model; and (iv) a nonlinear RD toy model that uses the linear solution but modifies it slightly to add a nonlinear qualitative behavior at early times. Those models are described in Sec. II. In Sec. III and Sec. IV we introduce the Bayesian framework and other statistical tools used to perform parameter inference and to assess the physical reliability of the models. In Sec. V, we perform Bayesian parameter inference on a set of zero-noise-realization NR signal injections for each of the models described in Sec. II. Finally we conclude about the accuracy and suitability of each model at describing the RD regime in Sec. VI.

II. RD MODELS

A. QNM overtone models

At late enough times, the RD regime can be modeled via the Teukolsky equation [81], which describes linear perturbations off a Kerr background spacetime, and hence tells us how GWs propagate as $s = -2$ gravitational perturbations. This equation is typically solved by applying outgoing boundary conditions at null infinity and infalling boundary conditions at the BH horizon. The Teukolsky equation then becomes an eigenvalue problem whose

¹The QNMs of Kerr do not form a complete basis even at linear order [73,74]. The time-domain Green’s function might be split into three different terms, namely, the quasinormal mode solution, the branch cut and a high frequency response. In particular, the prompt emission is originated from the branch cut solution and it is expected to be important at times around the peak of the emission (see [75] for a detailed review).

solution is the countably infinite set of the complex QNMs of the final (Kerr) BH. In a time evolution, these modes take the form of exponentially damped sinusoids. Their complex frequencies $\omega_{lmn} = w_{lmn} - i/\tau_{lmn}$, corresponding to poles of the Green function [23–25], are solely determined by the remnant BH’s mass M_f and spin a_f , in the absence of a BH charge. Here, $\text{Re}[\omega_{lmn}] = w_{lmn}$ are the so-called oscillation frequencies and $-\text{Im}[\omega_{lmn}] = 1/\tau_{lmn}$ are the damping rates (inverse of the damping times). These modes are labeled by three integers l , m , and n . Here $l = 2, 3, \dots$ and $m = -l, -l+1, \dots, l-1, l$ denote the two angular indices of the spheroidal harmonics decomposition. The complex strain at future null infinity $h = h_+ - ih_\times$ (where h_+ and h_\times denote the two polarization components measured in the detector frame) of the gravitational radiation is accordingly written as

$$h(t, \theta, \phi) = \sum_{l,m,n} h_{lmn}(t) {}_{-2}\mathcal{Y}_{lmn}(\theta, \phi; a_f), \quad (1)$$

where ${}_{-2}\mathcal{Y}_{lmn}(\theta, \phi; a_f)$ are the spin-weighted spheroidal harmonics of spin weight $s = -2$, which depend upon the polar angle θ , the azimuthal angle ϕ , and the final spin a_f . The third index, $n = 0, 1, 2, \dots$, labels the tones, in order of decreasing damping times τ_{lmn} for any given (l, m) harmonic. This convention sets the $n = 0$ (fundamental) mode as the dominant one at late times while the $n \geq 1$ mode (overtone) are shorter-lived. In addition, there are two branches of QNMs for each (l, m) harmonic, respectively with positive and negative w_{lmn} values [82]. The counter-rotating modes, with $w_{lmn} < 0$, are nevertheless, expected to have very small relative amplitudes in the dominant harmonics sourced by a quasicircular merger [32,83,84], and we shall not consider them further in this paper.

Methods to calculate numerical values of QNM frequencies are present in the literature [82,85–91] for various situations, building upon Leaver’s continued fraction method [23] or spectral decompositions [90,91]. In our work, we mainly use the open-source `qnm` Python package [89] to compute the required Kerr QNM frequencies as functions of the remnant’s mass and spin. Alternative open-source algorithms to compute the Kerr spectrum are also available in [85,92–94].

In this work, we focus on the dominant $(l = 2, m = 2)$ mode of the strain, $h_{22}(t)$, both in terms of the NR data we are considering and of the models used to describe it. Note that the mode we select from NR simulations is in fact the $(l = 2, m = 2)$ mode in a *spherical* harmonics decomposition, meaning that it includes some contributions from higher spheroidal harmonics (and the associated QNMs); in aligned-spins cases like we consider, there is in particular some mode mixing with the $(l \geq 3, m = 2)$ harmonic. Such contributions are expected to be negligible at all times due to the combination of much smaller amplitudes of these higher modes and small mixing coefficients, so that the spherical

$(2, 2)$ mode considered is a close approximation to the spheroidal one [66,84,95]. They might nevertheless affect analyses involving high overtones [64], as the small contributions from the fundamental modes ($n = 0$) of these other harmonics—like the $(l = m = 2, n = 0)$ dominant mode—are much longer-lived than those overtones. Furthermore, such mode mixing contributions may be enhanced in NR waveforms due to supertranslation caused by memory effects, which can possibly be solved by fixing the BMS frame [96]. We shall however leave such considerations for future work, and neglect mode mixing into the $(2, 2)$ spherical mode of the NR strain in the present analyses.

The decomposition of $h_{22}(t)$ into the $(l = 2, m = 2)$ QNMs up to a given number $N \geq 0$ of overtones defines the linear *overtone model* for the RD,

$$\text{OM}_N(t) = \sum_{n=0}^N \mathcal{A}_n e^{-i(t-t_r)\omega_{22n}}, \quad (2)$$

where t_r is a reference time, usually chosen as a sufficiently late point for the system to reside in the linear regime [36,37,65,97–100], and $\mathcal{A}_n = A_n e^{i\phi_n}$ is the complex amplitude of the $(l = 2, m = 2, n)$ tone at $t = t_r$. These $N + 1$ complex amplitudes, plus the final dimensionless mass and spin m_f, a_f which parametrize the QNM frequencies $\omega_{22n}(m_f, a_f)$, define the $2N + 4$ real-valued free parameters of the model. References [32,36] provide separate models of the overtone amplitudes and phases, calibrated to the progenitor parameters limited to $N = 1$, while an analogous calibration for $N > 1$ is still missing.²

This model provides *a priori* a good description of the RD once sufficiently into the linear regime, and while asymptotic late-time non-QNM linear tail contributions are still negligible.³ This model has been argued to be potentially applicable early on in the RD, up to the peak of the strain’s amplitude [66], for a sufficiently large N . We shall however also consider several alternative models including nonlinear terms, which may better capture the behavior of the strain close to merger.

²Reference [43] observes, by performing full Bayesian inference on the event GW150914, that the overtone model OM_1 with the phase ϕ_{221} fixed to the NR calibrated value is disfavoured in terms of the Bayes factor with respect to the OM_1 model in which A_{221}, ϕ_{221} are freely sampled, or not constrained to the NR fit values. This discrepancy might be sourced by the strong dependence of the value of the free phase ϕ_{221} on the ringdown starting time, as is remarked in [33].

³Such a tail contribution, with a non-oscillatory power-law decay, is indeed expected as an additional solution to the Teukolsky equation since QNMs do not form a complete solution basis [74–77,101]. Its amplitude is nevertheless small enough that this term only appears at very late times and is typically not visible within the post-merger time range of quasicircular NR simulations such as the ones we consider [64,75]. Such tail effects have only been observed very recently in eccentric mergers from NR, where they were expected to be enhanced compared to quasicircular cases [102].

B. Phenomenological nonlinear toy models

The first model with deviations to the linearized GR sum of QNMs that we consider, is based on the parametrized QNM models popular in spectroscopic studies, which allow for deviations of the QNMs to the Kerr spectrum. To avoid the very large parameter space and reduce the possible overfittings of models with multiple overtones that can each independently deviate from GR, we consider the restricted case where only the highest tone of the model is modified. This defines the highest-tone perturbation models (HTPM),

$$\text{HTPM}_N(t) \equiv \text{OM}_{N-1}(t) + \mathcal{A}_N e^{-(t-t_r)w_{22N}(1+\alpha_N)} e^{-(t-t_r)/(\tau_{22N}(1+\beta_N))}, \quad (3)$$

where α_N and β_N are respectively the oscillation-frequency and damping-time perturbation parameters. Their values measure the deviations of the highest included tone from the Kerr spectrum, and the QNM solution from GR would be recovered for $\alpha_N = \beta_N = 0$. HTPM_1 corresponds to the most widely used QNM model in overtone-based spectroscopy (e.g., [13,14,41,43,47]), including the 220 and 221 modes with possible frequency and damping times deviations to the Kerr values for the first overtone. $\text{HTPM}_{\geq 2}$ is a restricted extension of this model to higher numbers of overtones, where only the last tone is allowed to deviate from the GR spectrum. HTPM_0 is also formally well-defined by the above Eq. (3), but it has very limited interest due to the full degeneracy between the free final mass and spin and the deviation parameters on the complex frequency of the only mode present ($n = 0$), making it effectively an overparametrized version of OM_0 . We will accordingly not consider it in our analyses. Note that HTPM_N depends in total on $2N + 6$ real-valued free parameters (i.e., the same number as OM_{N+1}): the final mass and spin (M_f, a_f), the perturbation parameters α_N and β_N , and the complex amplitudes of the $N + 1$ tones included.

The other phenomenological toy model considered in this work amounts to a sum of QNMs with a nonlinear transformation of the time coordinate. The time parameter is shifted by an exponentially decaying term, so that the model can exhibit this nonlinear modification at early times close to merger (where it leads to a slower variation of the phase and amplitude of the waveform), while asymptotically recovering the linear model at later times⁴ We define the corresponding time coordinate transformation models (TCTM) as follows:

$$\text{TCTM}_N(t) \equiv \text{OM}_N(t + Ae^{-t/\tau}), \quad (4)$$

⁴Since the prompt response is expected to be higher close to the peak of the emission, the TCTM model is designed to account for this excess, although its fundamental form remains unknown. The TCTM may as well be interpreted as phenomenologically accounting for post-merger GWs from a BH of time-dependent mass and spin due to the absorption of the infalling radiation [103–105].

where A and τ are two constant parameters to be determined. Like in the HTPM case above, TCTM_N depends on $2N + 6$ real-valued free parameters: the final mass and spin, A , τ , and the $N + 1$ complex tone amplitudes.

We also considered several additional phenomenological toy models, introduced in [106] for the description of the decaying deformations of the final horizon formed in a merger. These models corresponds to overtone models modified e.g., by the addition of a non-oscillatory exponential decaying component [under the form $\text{OM}_N(t) + B \exp[-(t - t_r)/\tilde{\tau}]$], or of a power-law decaying term with or without oscillations [$\text{OM}_N(t) + C(t - t_1)^{-\gamma} \exp[i\omega(t - t_r)]$], or the same form with ω set to 0]. These models are designed to recover the steep decay featured by the deformations of the common horizon shortly after its formation, in addition to the late-time QNM oscillations. Hence, these models were not expected to be necessarily also well-suited to the description of ringdown waveforms at null infinity, which rather have a slower change of amplitude near the merger than further into the RD regime. Indeed, the preliminary comparative tests of the various models discussed in this section (see below in Sec. III D) indicated a poor performance for these additional models for the description of waveform ringdowns, and we did not consider them further for the present work.

C. IMR model

One can also use full inspiral-merger-ringdown waveform models to describe the GW ringdown, by selecting only the post-merger part of these models. They are built upon nonlinear ansatz, calibrated to NR waveforms, which depend solely on the progenitors' parameters. In general, they will require fewer input parameters than the overtone models, especially compared to those including a large number of overtones N_{max} . In this work, we use the nonprecessing “IMRPhenomD” waveform model. This model is calibrated to mass ratios up to $q = 1/18$ and initial effective spins up to 0.98 [107], and is well-sufficient to cover the 22 mode of nonprecessing cases; the only waveforms we consider in this work. Another advantage of using IMRPhenomD for this study is that it has been calibrated to a relatively small number of numerical waveforms, allowing us to easily pick a set of NR waveforms for the present study that were not involved in that calibration.⁵

We generate the IMRPhenomD using the PyCBC [109] time-domain approximant. We truncate the waveform at $t = 0$, aligning it with the peak of the strain for the 22

⁵We have also tested two other waveform approximants for comparison, namely IMRPhenomPv2 and SEOBNRv4, in the case of analyses starting at the strain amplitude peak ($t_0 = 0$), and found similar or better performances than IMRPhenomD. We chose IMRPhenomD in part because of the fact that more state-of-the-art approximants were usually calibrated to a much larger number of NR waveforms [16,20,108], and thus potentially exhibit artificial advantages in the model comparison.

mode. This alignment corresponds to a frequency $f_{\min} \sim 170$ Hz. We use a sampling rate $\delta t = 1/2048$ s, appropriate to resolve the high-frequency RD regime. We select only the 22 mode. The inclination angle is fixed to zero so that the complex strain is just $h_+ - ih_\times = h_{22}(t)_{-2} \mathcal{Y}_{22}(\theta, \phi)$. Note that we are comparing the IMRPhenomD model with NR waveforms, hence, we must translate the IMR output to geometric units with $G = c = M = 1$, which implies that the final mass referred in this work represents the fraction of energy radiated $M_f/M = 1$. With this setup, we are left with four free parameters in the model: mass ratio, χ_1^z, χ_2^z , and phase, where χ_1^z, χ_2^z denote the z component of the initial dimensionless spin of the progenitor BHs. Finally, the final mass M_f and final spin a_f are obtained from fits to NR in terms of the progenitor parameters [110,111].

III. MODEL COMPARISON

A. Mismatch analyses

While the bulk of our analysis is based on a full Monte Carlo sampling parameter estimation for each model, we first performed a least-mean-squares fit-based preliminary comparison and selection among the models at hand. The modeling quality can be assessed in this case using the mismatch \mathcal{M} . This quantity commonly used in GW astronomy to quantify the similarity between the model and data [65,97,99] is defined as

$$\mathcal{M} = 1 - \frac{\langle h_{\text{NR}} | h_m \rangle}{\sqrt{\langle h_{\text{NR}} | h_{\text{NR}} \rangle \langle h_m | h_m \rangle}}, \quad (5)$$

where we compare between our model for the strain 22 mode, $h_m(t)$, and the corresponding numerical data, $h_{\text{NR}}(t)$, with

$$\langle f | g \rangle = \text{Re} \int_{t_0}^{t_f} f^*(t) g(t) dt. \quad (6)$$

The limits of the integral t_0 and t_f mark the fit starting and ending time, respectively. \mathcal{M} varies between 0 and 1, with higher mismatches meaning that the model deviates more from data. We can thus compare models by computing the mismatch of each of them (with the best-fit parameter values) to the data. A lower value of that mismatch is associated with a more faithful modeling, without, at this stage, accounting for possibly different numbers of free parameters.

B. Bayesian framework

Apart from mismatches, another quantity of common use for comparing the fitting performance of different GW models is the Bayes factor. As opposed to the mismatch, the Bayes factor directly quantifies the relative evidence in favour of a model versus another given the data, and this

comparison already includes an implicit penalty cost for additional parameters and potential overfitting, through the prior and parameter space volume. It applies within a Bayesian parameter inference framework for each model \mathcal{M} , where the posterior probability distribution of the parameters $\vec{\theta}$ associated with the model, given the data d (here $d = h_{\text{NR}}$), is given by

$$p(\vec{\theta} | d, \mathcal{M}) = \frac{p(\vec{\theta} | \mathcal{M}) p(d | \vec{\theta}, \mathcal{M})}{p(d | \mathcal{M})}. \quad (7)$$

Above, $p(\vec{\theta} | \mathcal{M})$ is the prior probability of the parameters $\vec{\theta}$, $p(d | \vec{\theta}, \mathcal{M})$ is the likelihood function which represents the conditional probability of observing d given the model \mathcal{M} with parameters $\vec{\theta}$, and $\mathcal{Z} \equiv p(d | \mathcal{M}) = \int p(d | \vec{\theta}, \mathcal{M}) p(\vec{\theta} | \mathcal{M}) d\vec{\theta}$ is the evidence associated with model \mathcal{M} .

Two possible models \mathcal{M}_A and \mathcal{M}_B for the description of a given dataset d can then be compared by computing their relative Bayes factor, i.e., the ratio of evidence between them,

$$\mathcal{B}_{AB} = \frac{p(d | \mathcal{M}_A)}{p(d | \mathcal{M}_B)}. \quad (8)$$

As per usual practice, and for convenience, we will be using the logarithmic Bayes factor $\log_{10} \mathcal{B}_{AB}$, as well as the logarithmic evidence for any given model $\log_{10} \mathcal{Z}$ (the difference of logarithmic evidences between two models providing directly the logarithmic Bayes factor between them). Note that we use the base 10 log here. $\mathcal{B}_{AB} > 1$ ($\log_{10} \mathcal{B}_{AB} > 0$) would support model \mathcal{M}_A over model \mathcal{M}_B , and vice versa; although a significant claim of preference of \mathcal{M}_A over \mathcal{M}_B would require $\log_{10} \mathcal{B}_{AB} \gtrsim 1$ [112].

C. Bias analyses

Typically, both the best-fit mismatch and Bayes factor (with respect to a reference model) for each model are only used to assess the fitting quality, without accounting for the physical accuracy of the values obtained for the model parameters. This accuracy can be measured separately *via* the combined recovery bias ϵ on the final mass M_f and dimensionless final spin a_f [67,97],

$$\epsilon = \sqrt{\left(\frac{M_f^{\text{fit}} - M_f^{\text{true}}}{M} \right)^2 + (a_f^{\text{fit}} - a_f^{\text{true}})^2}, \quad (9)$$

where the final masses are normalized by the initial total mass M from the NR simulation. The true parameters M_f^{true} and a_f^{true} correspond to the values from the NR simulation, that are estimated from the mass and spin quasilocal definitions on the apparent horizon [67,80,113,114]. The

uncertainties of these final mass and spin local estimates from NR are typically in the order of 10^{-5} to 10^{-4} [67].

D. Preliminary tests

As a preliminary step to rapidly select relevant models and assess general trends, we fitted various models, with a range of numbers of tones, to the h_{22} ringdown strain mode from the BBH:0305 binary BH simulation from the SXS catalog [80]. The ringdown phase of the signal was selected by starting the analysis at the peak of the corresponding amplitude $|h_{22}|$ (which we use to define $t = 0$), i.e., by setting $t_0 = 0$; up to the end of the available data ($t_f/M \sim 150$). For the sake of stability and efficiency of the fits, we followed the same algorithm as in [67,92] to obtain the best-fit parameters for each model. The two to four parameters of a given model which are not tone amplitudes and phases (that is, for instance, $\{M_f, a_f\}$ for overtone models, and $\{M_f, a_f, A, \tau\}$ for the HTPM models) are distributed on an adaptive grid. For each value of those parameters on the grid, the best-fit value for the remaining parameters of the model, i.e., the tone complex amplitudes, on which the model depends linearly, is obtained through the analytic minimization of the sum of squared residuals for a linear model. The mismatch between the corresponding best-fit waveform and the NR waveform is computed for each grid point, and the optimal value for the ‘nonlinear’ parameters on the grid such as M_f

and a_f is then determined as the value minimizing the mismatch. Note that minimizing over the mismatch or over the sum of squared residuals, for any given set of parameters, gives equivalent results in the limit of small mismatches (or residuals).

In Fig. 1, we show the mismatch \mathcal{M} (left panel) and final mass/spin bias ϵ (right panel) of these best-fit solutions for the OM and the alternative TCTM and HTPM models, at various numbers of overtones. For each value of $N = 1 \dots 7$ on the x axis, we show the results for the OM_N , $TCTM_{N-1}$, and $HTPM_{N-1}$ models (plus OM_0 for $N = 0$), for direct comparison of models which have the same number of free parameters, i.e., $2N + 4$. We also considered the IMRPhenomD model, which has four parameters like the OM_0 ; we represent its mismatch and bias as a reference magenta horizontal dashed line and shaded area on each panel. The estimated numerical error on the mismatch and bias parameter are also shown as dark gray horizontal lines and shaded areas.

These comparison plots show that the TCTM (at any N) and the HTPM (from $HTPM_1$ onwards) provide a comparable or (in most cases) better description in terms of mismatch to the ringdown 22 mode of SXS:BBH:0305, than the OMs for the same number of free parameters. On the other hand, these two classes of models typically recover more poorly the parameters of the final BH than the corresponding overtone model, with the notable exception of $TCTM_1$ and $TCTM_2$ (compared to $OM_{2,3}$); while

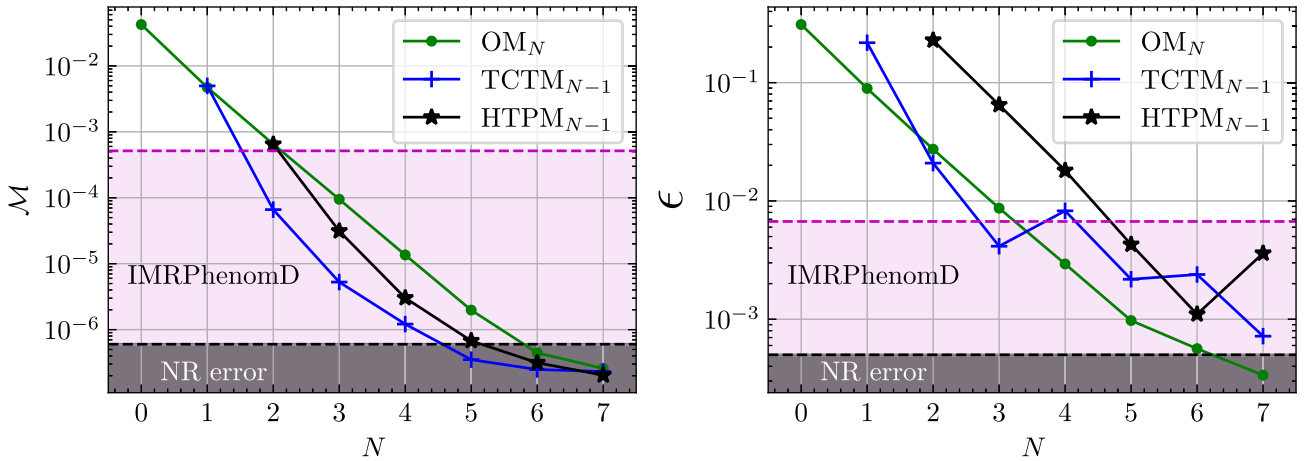


FIG. 1. In the left panel, we show the evolution with $N \in \{0, \dots, 7\}$ of the mismatch \mathcal{M} between the NR waveform and the best-fit OM_N , $TCTM_{N-1}$ and $HTPM_{N-1}$ models (discarding the over-parametrized model $HTPM_0$). For a given N (along vertical lines on the figure), these models have the same number ($2N + 4$) of free parameters and can thus be directly compared. The NR ringdown waveform considered here corresponds to the BBH:0305 simulation from the SXS catalog, selecting the 22 mode and starting at its amplitude peak ($t = 0$). In the right panel, the evolution with $N \in \{0, \dots, 7\}$ of the bias parameter ϵ is presented for the same models. The magenta dashed line and shaded area in each panel mark the optimal mismatch and bias obtained for the IMRPhenomD model, which has four free parameters like the OM_0 ($N = 0$) model. The dark gray dashed line and shaded area at the bottom of each panel delimit the mismatch and ϵ values that are lower than the estimated NR errors, i.e., the maximum of the mismatches $\max(\mathcal{M}_{\text{res}}, \mathcal{M}_{\text{extr}})$ and the total discrepancy $\delta\epsilon_r$ on the dimensionless radiated energy and angular momentum, obtained from comparing the two highest available resolutions and from comparing the two best extrapolation orders for the 22 mode of the NR waveform (see Sec. III-B of [67]). Note that the minimum grid resolution used for the recovery of M_f/M and a_f for the OM, HTPM and TCTM models was $|\delta M_f|/M, |\delta a_f| = 3.2 \times 10^{-6}$ for both parameters, and hence has a negligible impact on the ϵ values obtained.

like for the overtone models the bias does decrease in most cases when more tones are included in the model. Finally, the four-parameter IMRPhenom model provides a description of the NR data of a quality comparable to the eight-parameter OM_2 and HTPM_1 models (and better than the six-parameter TCTM_0), with a much lower bias on the final mass and spin. For this model, a good fitting quality could be expected to some extent, thanks to its prior calibration to other NR waveforms including times around the strain peak ($t = 0$). Notice, however, that the calibration of IMR approximants is performed and tested as a full inspiral-merger-ringdown model, with its accuracy tested as a whole too. Therefore, the accuracy and performance of the ringdown part alone, is not fully guaranteed *a priori*, especially the good recovery of the final black hole parameters that we find here.

The few other phenomenological RD models, not shown here, that we considered in this preliminary study (e.g., adding a non-oscillatory damped power-law or exponential term to a sum of QNM overtones) were typically performing much more poorly in both mismatch and bias than the models shown, and are consequently not considered further in this work.

We shall now focus on the models with low or moderate numbers of parameters which showed comparable or better performance than the first few overtone models, i.e., $\text{OM}_{0\dots4}$, $\text{TCTM}_{0\dots2}$, $\text{HTPM}_{1,2}$, and IMRPhenomD , for a more thorough comparison in a Bayesian inference approach using nested sampling [115].

IV. PARAMETER ESTIMATION

For GW detectors, the frequency-domain likelihood function under stationary Gaussian noise is defined from the noise-weighted frequency-domain inner product (\cdot, \cdot) as follows [116]:

$$p(d|\vec{\theta}, \mathcal{M}) = \exp \left[-\frac{1}{2} (d(f) - m(\vec{\theta}, f), d(f) - m(\vec{\theta}, f)) \right], \quad (10)$$

where $m(\vec{\theta}, f)$ denotes the strain 22 mode from model \mathcal{M} with particular parameters $\vec{\theta}$, evaluated at frequency f , and d is the sum of the GW strain and the noise realization [117] for the 22 mode. The inner product (\cdot, \cdot) itself is defined from the one-sided power spectral density $S_n(f)$ of the detector's noise, as

$$(x, y) = 4 \times \text{Re} \int_0^\infty \frac{x^*(f)y(f)}{S_n(f)} df. \quad (11)$$

In our case, the parameter estimation is performed on time-domain data, with the NR ringdown 22-mode strain as our data set $d(t)$, considered as being injected in a zero-noise realization. We moreover consider here a flat noise

spectrum within the relevant frequency range, i.e., that the noise sensitivity curve can be approximated by its value at the frequency of the (220) mode [86], $S_n(f) \approx S_n(f_{220}) = cst$. This assumption allows us to directly relate this constant noise amplitude to the optimal ρ of the data, with $\rho^2 = (d(f), d(f)) = 2 \langle d(t)|d(t) \rangle / S_n(f_{220})$, and to convert more generally, via Parseval's theorem, the noise-weighted frequency-domain inner product (\cdot, \cdot) of Eq. (11) into the time-domain scalar product of Eq. (6),

$$(x(f), y(f)) = 2 \frac{\langle x(t)|y(t) \rangle}{S_n(f_{220})} = \rho^2 \frac{\langle x(t)|y(t) \rangle}{\langle d(t)|d(t) \rangle}. \quad (12)$$

The likelihood expression, Eq. (10), can thus be reexpressed in time domain as

$$p(d|\vec{\theta}, \mathcal{M}) = \exp \left[-\rho^2 \frac{\langle d(t) - m(\vec{\theta}, t)|d(t) - m(\vec{\theta}, t) \rangle}{2 \langle d(t)|d(t) \rangle} \right]. \quad (13)$$

We can therefore directly set the optimal ρ in our parameter estimations through the likelihood function, which for a given data d is equivalent to setting the constant noise amplitude within this approximation.

To perform parameter estimation and both obtain posterior distributions and calculate the models' Bayesian evidences, we use the dynamical nested sampling method from the *dynesty* Python package [118]. One particular feature of this method is that it estimates the evidence and the posterior simultaneously. Throughout our tests, we used 2000 live points and a stopping criterion of $\Delta(\ln \mathcal{Z}) = 0.1$ for the nested samplings.

V. RESULTS

We start our initial inference analysis on the GW150914-like simulation, SXS:BBH:0305, employing the parameter estimation framework this waveform into white Gaussian noise, simulating an event observed by third-generation (3G) observatories with a signal-to-noise ratio of $\rho = 100$. SXS:BBH:0305 is consistent with a signal with mass-ratio $q = m_1/m_2 = 1.22$, effective dimensionless spin $\chi_{\text{eff}} = (\chi_1 m_1 + \chi_2 m_2)/(m_1 + m_2) = 0.01$. Our Bayesian inference is performed using four RD models described in Sec. II. Further details on the various prior choices for each RD model and their impact on the obtained posterior distributions are provided in Appendix A.

A. Bayes factor analysis for $t_0 = 0$

We initiate our parameter estimation (PE) analysis at $t_0 = 0$, i.e., consistent with the peak of the strain. We first estimate the values of the evidence \mathcal{Z} for each of the models considered here. The results of these runs are shown in Table I. We can deduce from the results that the IMRPhenomD model yields the highest value for

TABLE I. The table contains \log_{10} evidences, and remnant properties recovery biases corresponding to the maximum-likelihood values of the samplings, for the 11 models considered here, for the GW150914-like simulation waveform SXS:BBH:0305 from the SXS Collaboration. The sampling is performed using the *dynesty* Python package. The number of free parameters of each model is also given in the second column. Noteworthy, we have found that at $\rho = 100$ as we used here, the value of ϵ is mildly subjected to finite-sampling uncertainties.

Model	Parameters	$\log_{10} \mathcal{Z}$	ϵ
OM ₀	4	-188.435	0.311261
OM ₁	6	-31.9132	0.087670
OM ₂	8	-17.0332	0.027019
OM ₃	10	-17.1311	0.011475
OM ₄	12	-17.7541	0.032821
TCTM ₀	6	-33.2123	0.216384
TCTM ₁	8	-14.4255	0.024559
TCTM ₂	10	-14.2678	0.004472
HTPM ₁	8	-17.1984	0.236650
HTPM ₂	10	-17.3353	0.096609
IMRPhenomD	4	-9.57672	0.014981

$\log_{10} \mathcal{Z}$, suggesting a better fit to the NR data compared to the other models. Moreover, among the nonlinear models examined in this study, the second and third highest-ranking models in log evidence are the nonlinear TCTM models. Specifically, the TCTM₂ yields a log Bayes value of $\log_{10} \mathcal{B} \sim 3$, indicating that it is approximately $\mathcal{O}(10^3)$ times larger than the log evidence for the overtone solutions OM₂ and OM₃. Notably, the TCTM₂ achieves this superior performance while having the same number of parameters as the latter. We also observe that, among the linear solutions, the $\log_{10} \mathcal{Z}$ saturates at OM₂ and it provides a slightly lower value for OM₃. We verified that the $\log_{10} \mathcal{Z}$ value consistently decreases for OM₄ and OM₅ thus, showing that the optimal performance of the OM models occurs at OM₂. This is compatible with the overtone-models results of [64] and—in the complementary context of deformations of the final horizon—of [72]. Finally, the non-GR model HTPM₁ provides similar $\log_{10} \mathcal{Z}$ as OM₂.

To ensure the robustness of these results and rule out potential influences from varying prior choices, we have examined and confirmed that adjusting priors does not qualitatively alter these findings. The results shown for different prior choices is shown in Appendix A. Therefore, and from the Bayes factors' point of view, the nonlinear models are preferred for the waveform SXS:BBH:0305.

In the fourth column of the same table, we show the mass/spin recovery bias ϵ as defined in Eq. (9) for the ten models considered. The true values $M_f^{\text{true}}, a_f^{\text{true}}$ are obtained from the NR metadata files, while the $M_f^{\text{fit}}, a_f^{\text{fit}}$ correspond to the maximum likelihood values obtained after sampling the likelihood distribution of Eq. (13). The biases on the final mass and the final spin for the OM models improve

gradually from OM₀ to OM₃, and it starts to degrade for OM₄ (consistently with the overtone-models analyses of [64]). Notice that this last result slightly differs qualitatively from the analysis we have done based on the value of the evidence \mathcal{Z} . This is expected since the computation of the evidence provides an extra penalty factor to the increase of the prior volume, which in this case is sourced by the large number of free parameters of the high- N OM models. Moreover, we find some mild disagreements between the values of ϵ obtained in Fig. 1, with respect to the ones listed in Table I, especially for the models with a high number of overtones, leading to a different behavior for OM₄. Figure 1 is obtained by nonlinear minimization to fit the NR data, with the precision of ϵ fixed by the mass-spin grid resolution. Therefore, data overfitting/underfitting may happen with such prescription. On the contrary, the results shown in Table I are obtained from sampling the whole $(2N + 4)$ -dimensional likelihood distribution, which involves a larger exploration of the parameter space. This reduces the risk of overfitting the data and thus provides a more statistically robust representation of the recovery biases. The statistical uncertainties of ϵ , at the SNR we consider here ($\rho = 100$), will be better illustrated in the next subsection.

Regarding the nonlinear models, we obtain a slightly larger bias for the nonlinear IMRPhenomD model than for OM₃, $\epsilon^{\text{IMRPhenomD}} \gtrsim \epsilon^{\text{OM}_3}$, while the evidence \mathcal{Z} for the IMRPhenomD is much larger. The higher Bayesian evidence for this particular model is due in part to its calibration to a set of NR waveforms (which does not include SXS:BBH:0305), which allows it to depend only on the few parameters characterizing the progenitor BHs: mass ratio, magnitudes of both aligned spins, orbital phase. It was not, however, separately calibrated to the ringdown phase, and the still rather good recovery of the final BH parameters from the whole ringdown (starting at the $t = 0$ amplitude peak) that we obtain was not fully ensured by design. The best model in terms of (M_f, a_f) bias is the other nonlinear model TCTM₂, with $\epsilon = 0.0045$.

B. Mass and spin posterior distributions for $t_0 = 0$

We study the marginalized posterior distribution of remnant properties for each of the models considered in this work. Notice here that the posterior distribution of IMRPhenomD are originally q, χ_{1z}, χ_{2z} , which are parameters of the progenitor BHs. Thus, these are converted to the final state parameters using NR fits to the final BH state [109–111].

In Fig. 2, we show the final mass and final spin posterior distributions for the models OM_{0–3} and IMRPhenomD (in magenta). The “+” symbols, represent the maximum likelihood values for each of the models considered, and that correspond to the values of ϵ shown in the fourth column of Table I. Notice that the posterior distributions on the final mass and the final spin are consistent with the true

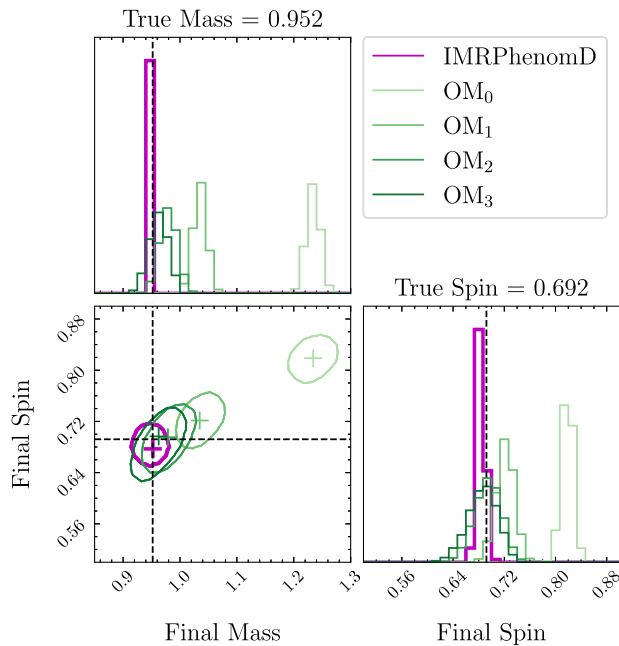


FIG. 2. We show the comparison of final mass and spin posterior distribution for the sampling of OM_{0-3} and IMRPhenomD for waveform SXS:BBH:0305. Each contour represents a 90% credible region on the mass-spin 2D plane for given model. The black dashed lines note the “true” final mass and spin. The “+” signs denote the maximum likelihood values for each of the models considered. We assume the injection SNR ρ to be 100 for all the cases, in order to see the clear comparison. Notice that the 2D marginalized distributions for OM_2 and OM_3 are practically overlapping, thus showing no significant performance gain for the OM_3 . Note that we observe a significant overlap between the contours of OM_3 and OM_4 . Since we also see in Table I no gain in Bayesian evidence and recovery bias when including more than 3 overtones, OM_4 is excluded for the clarity of this plot.

parameters for the models with $OM_{n \geq 2}$, while it shows large offsets for the models $OM_{n=0,1}$. Moreover, it is noteworthy that the 90% credible contours increase slightly with the overtone index, from $n = 0$ to $n = 3$. The broadening of the posterior contours might be sourced by the observed correlations among the tones (see the Appendix B of [65]), which become especially relevant for tones with $n \gtrsim 1$. Therefore, the precision at which one can measure the final mass and final spin for signals at $\rho = 100$ using OMs reaches a maximum for $n = 2$ and it slightly degrades for $n > 2$. Alternatively, notice that the IMRPhenomD model provides (i) lower values for the bias ϵ than the best OM solution, and (ii) tighter mass and spin contours than all the other models considered. Therefore, we observe that the IMRPhenomD model provides a more accurate description of the signal from $t_0 = 0$ than the OM models, both if one uses the Bayesian evidence as a ranking criterion, and from testing the consistency of the posterior distributions with respect to the true parameters.

In Fig. 3, we show the posterior distributions of the final mass and the final spin for the models OM_2 , TCTM₁,

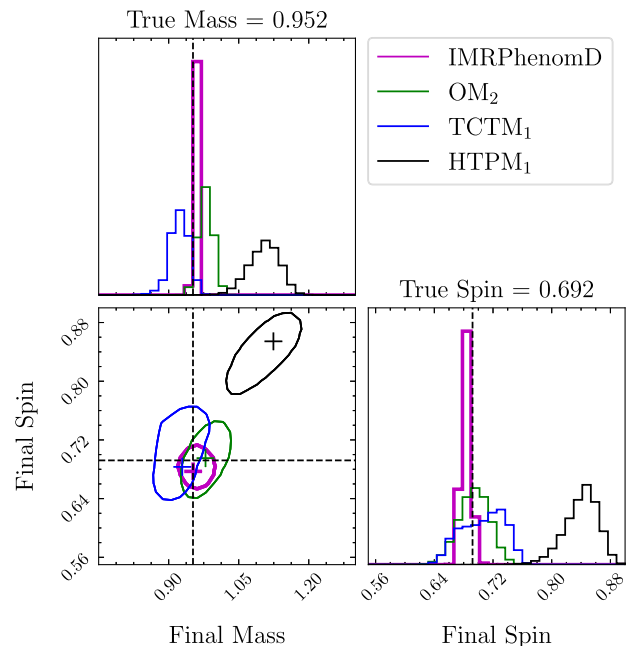


FIG. 3. We show the comparison of final mass and spin posterior distribution for the sampling of OM_2 , TCTM₁, HTPM₁, and IMRPhenomD for the NR waveform SXS:BBH:0305. Each contour represents a 90% credible region on the mass-spin 2D plane for a given model. The black dashed lines note the “true” final mass and spin. The “+” symbols represent the maximum likelihood estimated for each of the models considered in this work. We assume the injection SNR to be 100 for all the cases, in order to see the clear comparison.

HTPM₁, and IMRPhenomD for the same waveform at $\rho = 100$. We compare the inferred posterior distributions of the optimal linear model OM_2 with all the other nonlinear models. Notice that the 90% credible contours of the nonlinear IMRPhenomD model still provide tighter constraints on the remnant parameters and a lower value for the bias ϵ . It is noteworthy that IMRPhenomD is characterized by only four parameters, distinguishing itself from all the other models under consideration, each of which involves eight parameters. Another interesting observation is that even though TCTM₁ has better Bayes evidence compared to the corresponding OM_2 (i.e., having the same number of parameters), both its posterior distributions and its values for the ϵ are still compatible to each other. Notably, the model exhibiting the least favorable performance is HTPM₁, displaying a significant bias (approximately 0.2) in relation to the true values. This bias arises from the model’s flexibility in deviating from GR and from the mismodeling of the early time features by the GR-only OM_1 model, resulting in a looser and biased constraint on the remnant mass and spin values. Significantly, the model HTPM₁ is presently employed for conducting GR tests in the analysis of ongoing events observed by the LVK Collaboration thus, the use of this model might be limited

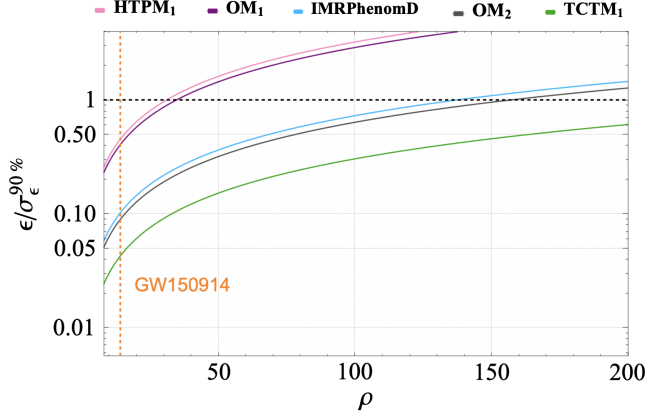


FIG. 4. The plot illustrates the ratio of the expected bias or systematic error ϵ to its 90% credible interval statistical error σ_ϵ for each of the models examined in this study. The black dashed line, denoted by $\epsilon/\sigma_\epsilon \gtrsim 1$, signifies the point at which systematic error begins to dominate over statistical error. Notably, the models HTPM₁ and OM₁ cross this threshold at RD $\rho \approx 30$, a region that may soon be reachable by current observatories or upcoming ones such as A#. The orange dashed line corresponds to the RD ρ value of the first event, GW150914.

to low ρ scenarios, in which the statistical errors dominate the systematic ones. To this aim, in Fig. 4 we have quantified impact of the systematic errors with respect to the statistical ones. In particular, we have estimated the ratio between the systematic error ϵ and the statistical one $\sigma_\epsilon^{90\%}$ estimated at the 90% percentile, $\epsilon/\sigma_\epsilon^{90\%}$, in terms of the SNR ρ . Notice that the quantity $\epsilon/\sigma_\epsilon^{90\%}$ helps one identify the SNR domain in which the systematic errors dominate, rather than providing any ranking based on the performance of the various models used in this work, since low values of this ratio favor large statistical uncertainties as much as low-systematic errors. We note that the applicability of HTPM₁ and OM₁ appear to approach their limit around RD $\rho \approx 30$. At this point, the influence of systematic errors begins to overtake the statistical uncertainties in the inference of mass and spin values (combined in the variable ϵ). Yet, the prevailing the statistical uncertainty evident in present events, driven by the noise sensitivity of observatories, notably outweighs the parameter biases identified in this study. However, as demonstrated in our study, the accurate determination of the final mass and spin would become predominantly influenced by the systematic errors for the linear models currently used in ringdown parameter estimations (for LVK events) HTPM₁ and OM₁, when confronted with the anticipated high- ρ scenarios characteristic of third-generation observatories. A much larger $\rho > 120$ is required for the simple nonlinear models IMRPhenomD and TCTM₁, which show enough accuracy to address the 3G requirements at high ρ . An analogous analysis for the waveform Ext-CCE:BBH:0002 is presented in Appendix B.

C. Dependence on the starting time t_0

Usually, there is a trade-off in truncating the waveform at different starting times. On the one hand, performing BH spectroscopy at late times RD leads to large statistical uncertainties due to the rapid decay of the SNR.⁶ On the other hand, starting the spectroscopic analysis close to the peak amplitude of the strain, results in a biased estimation of the parameters. This bias stems from the absence of modes in the OMs and potentially ignoring the nonlinear effects [68,78,119].

Here, we vary the fit starting time by truncating the waveform at different t_0/M , and we analyze the results in terms of the Bayes factor. We repeat the analysis for a set of starting times $t_0/M = -5, -2.5, 0, 2.5, \dots, 20$, where negative t_0/M include part of the waveform slightly before merger. The runs have been performed for the models OM₂, OM₃, TCTM₁, HTPM₁, and IMRPhenomD with reference ($t_0 = 0$) SNR⁷ $\rho_{t_0=0} = 100$. In Fig. 5 we show the \log_{10} Bayes factors for each model with respect to the OM₃ model via Eq. (8). We have found that the two nonlinear models considered in this work, IMRPhenomD and TCTM₁, provide positive log Bayes factors over OM₃, while the linear models OM₂ and HTPM₁ provide negative log Bayes factors around the merger (for negative and low positive t_0/M values). In particular, the Bayes evidence values we have obtained strongly support the IMRPhenomD model over OMs at early starting times, including before the waveform amplitude peak,⁸ and up to $t_0/M = 15$. This suggests that the nonlinear perturbations or even the prompt response effects could still dominate a short time after the merger. However, OM₂ consistently exhibits a comparable performance compared to all other models starting from $t_0 = 15$ onward, as the truncated waveform transitions into the linear regime.

D. Can we observe the high-overtone amplitudes?

The confidence statistical observation of a tone solely from the RD regime, requires that the inferred value of its amplitude must be incompatible with zero, at least, within a

⁶The SNR ρ scales inversely with the parameter uncertainty σ_λ as $\rho \sim 1/\sigma_\lambda$. As a rule of thumb, $\rho(t_0 = 0)/\rho(t_0/M = 10) \sim e^{-1} = 0.37$, which implies that the posterior distributions on the physical parameters at $t_0/M = 10$ are about e times larger than the ones obtained at $t_0 = 0$.

⁷Note that the actual SNR also relies on the choice of fit starting time t_0 . Truncating and fitting the waveform from the peak can result in larger ρ compared to fitting with only the later time of data. In order to make sure we consider the same event, we fix $\rho = 100$ at $t_0 = 0$ and let the other $t_0 \neq 0$ SNR ρ scaled with respect to the truncated waveform length.

⁸We note that both nonlinear models considered are strongly preferred over the linear ones (OM₂, OM₃, HTPM₁) at times slightly before the peak, $t_0/M = -5, -2.5$. This is not very surprising for IMRPhenomD which is designed to consistently model pre and post-merger phases, but it also holds, with lower evidences, for the nonlinear TCTM₁.

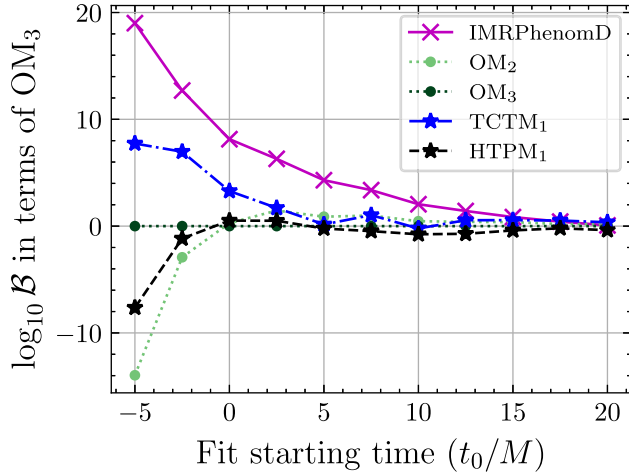


FIG. 5. We show the evolution of $\log_{10} \mathcal{B}$ with respect to OM_3 for 4 different models, OM_2 , TCTM_1 , HTPM_1 , and IMRPhenomD (as well as the reference OM_3 at $\log_{10} \mathcal{B} = 0$ by construction) at an assumed SNR $\rho = 100$, for a range of starting times $-5 \leq t_0/M \leq 20$, including times slightly before the amplitude peak ($t_0/M = -5, -2.5$).

given confidence level per tone amplitude C_n . Here, we use the one-sided 90% confidence value $C_n^{90\%}$ to assert the confident observation⁹ of a tone at a given SNR ρ for the NR waveform SXS:BBH:0305 [32]. In particular, we study the dependence of the magnitude $A_n/C_n^{90\%}$ for a set of SNRs injections with a network SNR $\rho \in [10, 100]$, where A_n provides the real-valued amplitude of the tones. An approximated observation of a tone would correspond to $A_n/C_n^{90\%} \sim 1$. To estimate $C_n^{90\%}$ we use the framework described in Sec. IV, where we also use the best fitting values of the amplitudes and phases obtained at t_0 . In Fig. 6 we show the quantity $A_n/C_n^{90\%}$ in terms of the SNR ρ for two of the OMs considered in this work; $N_{\max} = 2$ (top panel) and $N_{\max} = 3$ (bottom panel). The dashed vertical orange line corresponds to the post-peak SNR of GW150914 [41,43]. Notice that for each tone amplitude, the SNR required to cross one is larger as the n index increases. This is because as n increases the corresponding damping time of each tone τ_n decreases, thus carrying out a lower per-tone ρ . Specifically, $\rho_{n=1}(A_0/C_0^{90\%} = 1) > \rho_{n=1}(A_1/C_1^{90\%} = 1) > \rho_{n=2}(A_2/C_2^{90\%} = 1) > \rho_{n=3}(A_3/C_3^{90\%} = 1)$. Moreover, notice that $\rho \sim 30 - A_2/C_2^{90\%} = 1$ —is required for the full and confident observation of the $N_{\max} = 2$ model while $\rho \sim 80 - A_3/C_3^{90\%} = 1$ —is expected if $N_{\max} = 3$. A RD with $\rho \sim 30$ might be observed in the LIGO A# while for $\rho \sim 80$ is

⁹The posterior amplitudes, denoted as A_n and obtained from running PE are typically constrained to be positive based on our chosen priors. This imposes a stringent requirement on the lower limit, specifically, that $C_n^{90\%}$ must be greater than zero. In this context, the one-sided $C_n^{90\%}$ is determined by assuming a Gaussian symmetry around the peak value, making it approximately equivalent to the upper bound of the 90% confidence interval.

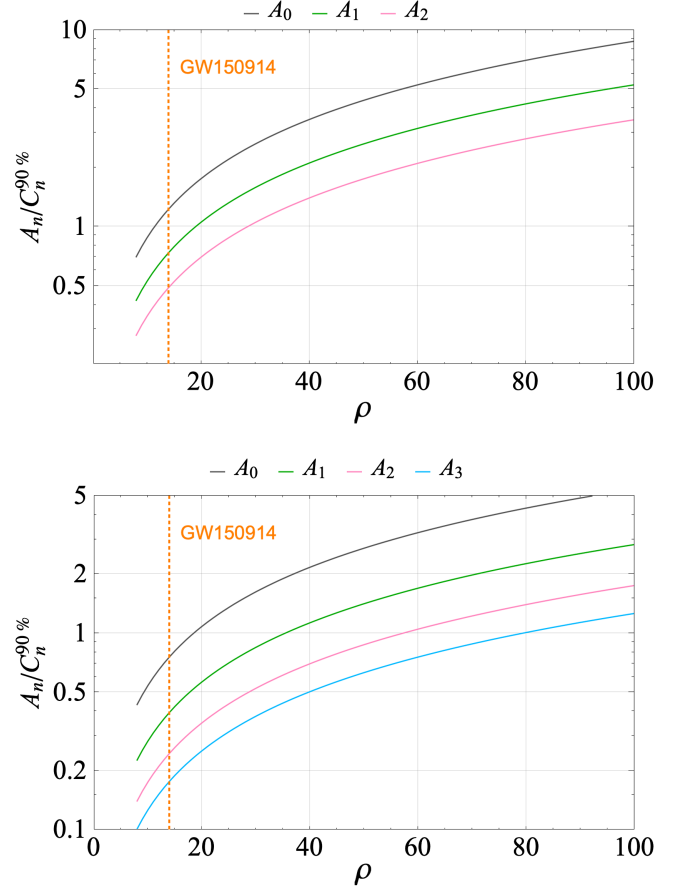


FIG. 6. Ratio $A_n/C_n^{90\%}$ of each tone's best-fit amplitude A_n to its 90% confidence interval, in terms of the simulated SNR for the GW150914-like waveform SXS:BBH:0305. The top panel represents $A_n/C_n^{90\%}$ for the OM_2 i.e., with $N_{\max} = 2$, and in the bottom panel we show the same results but for $N_{\max} = 3$. We take as a reference for observability $A_n/C_n^{90\%} \sim 1$. The vertical-orange dashed line provides the post-peak SNR of GW150914, corresponding to a starting time $t_0 = 0$.

expected to occur only for 3G observatories as ET and CE [59,61]. However, a significant concern with the high-order overtone models lies in the pronounced variation of tone amplitude when altering the number of tones, denoted as N_{\max} in the models [65,97]. For instance, the amplitude ratio between the amplitudes obtained from the fits to the NR data and for the $N_{\max} = 2, 3$ models varies as $A_n^{N_{\max}=3}/A_n^{N_{\max}=2} = \{1.04, 1.50, 3\}$ for the tones $n = 0, 1, 2$, respectively, from the fits to the NR data. The substantial variability, on the order of $\mathcal{O}(2-3)$, in the amplitude values for tones $n = 1, 2$ poses a challenge in determining whether these values represent the system faithfully or are influenced by other fitting systematics, such as the absence of tones or the presence of nonlinearities. Conversely, the value of the fundamental tone amplitude A_0 remains almost constant regardless the number of tones considered in this example. These amplitude variation results are consistent with, e.g., [64,67,120].

TABLE II. The table contains $(\log_{10} \mathcal{Z}, \epsilon)$ calculated for models IMRPhenomD, OM₂, OM₃, TCTM₁ and HTPM₁, at $\rho = 100$. They are sampled using the *dynesty* Python package for five binary BH merger NR waveforms from both the main and Ext-CCE catalog in SXS. The properties of the initial BH binary in each case, i.e., the mass ratio and the two dimensionless spins are also given. Notice here that the OM₂ always provides a similar/slightly better evidence than OM₃, which is consistent with the results already obtained for SXS:BBH:0305.

Catalog	Waveform	q	$\chi_{1,z}$	$\chi_{2,z}$	IMRPhenomD	OM ₂	OM ₃	TCTM ₁	HTPM ₁
Main	BBH:0150	1	0.2	0.2	(−8.215, 0.0080)	(−19.916, 0.0283)	(−22.449, 0.0095)	(−14.771, 0.0119)	(−19.314, 0.2059)
	BBH:0305	1.221	0.33	−0.44	(−9.558, 0.0150)	(−17.032, 0.0270)	(−17.121, 0.0115)	(−14.447, 0.0246)	(−17.208, 0.2367)
	BBH:1221	3	0	0	(−7.988, 0.0074)	(−16.652, 0.0494)	(−18.539, 0.0456)	(−15.071, 0.0503)	(−15.944, 0.2531)
	BBH:0300	8.5	0	0	(−6.207, 0.0092)	(−17.000, 0.1209)	(−18.583, 0.0851)	(−15.456, 0.0323)	(−15.647, 0.3011)
Ext-CCE	BBH:0002	1	0.2	0.2	(−44.57, 0.0238)	(−80.87, 0.0282)	(−81.44, 0.0238)	(−77.01, 0.0592)	(−79.67, 0.1880)

E. Analysis on different NR waveforms

To assess the robustness of our findings, we conduct parameter estimation using a distinct set of NR waveforms sourced from the SXS catalog. These waveforms, namely, SXS:BBH:0150, SXS:BBH:0300 and SXS:BBH:1221, cover a spectrum of mass ratios spanning 1, 3, 8.5 and effective spins of 0.2, 0, 0. We also append waveform Ext-CCE:0002 from the Ext-CCE catalog to the list, with the detailed discussion presented in Appendix B. Notice that these waveforms, as well as SXS:BBH:0305 considered so far, were not used to calibrate IMRPhenomD [107], thus are not biasing our model comparison. In Table II we show the \log_{10} Bayes evidence and biases ϵ for a selected set of models, i.e., IMRPhenomD, OM₂, OM₃, TCTM₁ and HTPM₁ for all NR waveform truncated at a starting time $t_0 = 0$.

We observe that IMRPhenomD consistently provides Bayes factors of approximately ~ 10 over OMs at $\rho = 100$, which denotes a clear preference for the nonlinear IMRPhenomD model compared to linear RD models. In addition, the nonlinear model TCTM₁ emerges as the second best solution based on the Bayes evidences, showing a considerable advantage over the OMs. In particular, notice that we do not observe significant differences on the values of $\log_{10} \mathcal{Z}$ for the OM₂ and OM₃, indicating that OM₂ provides a sufficiently accurate solution at $t_0 = 0$, consistent with the results observed for SXS:BBH:0305. While the non-GR model HTPM₁ offers log evidence values similar to those of the OM models.

Regarding the bias analysis, we have found that the IMRPhenomD model recovers the minimum value for ϵ , for the waveforms SXS:BBH:0150, SXS:BBH:0300, and SXS:BBH:1221. TCTM₁ appears as the second best model with comparable/better epsilon values comparing to the OM₂ and OM₃. And HTPM₁ generally performs the poorest in recovering the true final parameters as expected, which is similar as the case we have seen for SXS:BBH:0305 analysis. Therefore, at $\rho = 100$, for the five different NR waveforms tested here, we consistently observe the compelling preference for the nonlinear models compared to the OM models and non-GR model.

VI. CONCLUSIONS

In this work we have tested the performance of several RD models by fitting them to the 22 mode of quasicircular, nonprecessing NR waveforms. The models we have used to fit the NR data are divided into four categories: (i) The nonlinear RD regime of the IMRPhenomD approximant, which has been widely used in GW data analysis; (ii) the RD model as described by linear QNMs, dubbed here as OM; (iii) a family of nonlinear RD toy models, the TCTMs, which expand upon the linear models by including further qualitative nonlinear contributions; (iv) the HTPM models, which are linear but allow for deviations of the QNM spectrum from GR. Our results are obtained on NR waveforms of different nature: four extracted at finite radii and extrapolated to null infinity—labeled SXS:BBH:#—and one extracted through the Cauchy characteristic procedure, thus, with lower expected errors than the extrapolated ones, and labeled as Ext-CCE:BBH:0002. We first analyze the performance of the models at fitting the 22 mode of the waveform SXS:BBH:0305, at a starting time $t_0/M = 0$ (corresponding to the peak of amplitude of the 22 mode). We obtain the minimum mismatch \mathcal{M} and the bias ϵ on the recovered physical parameters of the remnant BH for all the models considered and over a range of maximum number of tones included in the models. We observe that the nonlinear TCTM models provide in general a lower mismatch than the overtone ones, even for $N_{\max} = 7$, while the IMRPhenomD post-peak model has a match to the data comparable to the eight-parameter $N_{\max} = 2$ OM model despite relying on only four free parameters. Regarding the final mass and spin recovery, we find that the nonlinear models IMRPhenomD and TCTMs both show a similar accuracy to the OMs up to $N_{\max} \sim 3$, while the OM solution outperforms them at $N_{\max} \gtrsim 3$. Next, we have also performed injections of the NR waveform SXS:BBH:0305 in zero-realization white Gaussian noise at SNR $\rho = 100$ and at different starting times $t_0/M \in [-5, 20]$, simulating the expected SNRs of the third-generation gravitational wave observatories such as the Cosmic Explorer and Einstein Telescope. We first note that the nonlinear model IMRPhenomD provides tighter constraints on the final mass and spin parameters at $t_0 = 0$

than the OM, even for $N_{\max} = 3$. In particular, $N_{\max} = 2$ and 3 provide compatible but broader mass and spin contours with IMRPhenomD albeit with a significantly lower Bayes evidence, while the $N_{\max} = 0, 1$ OM models are more biased, which is consistent with the results shown in [43]. Remarkably, there is currently no amplitude and phase overtone model calibrated to the BBH progenitor masses and spins for $N_{\max} > 1$ [32,36,120], which contributes to the broader $N_{\max} = 2, 3$ OM constraints. If such a model were to be developed, the additional uncertainty introduced by the calibration process might be expected to further broaden the amplitude and phase uncertainties, potentially compromising the accuracy compared to the IMRPhenomD model.

Moreover, we have computed the \log_{10} Bayes factor of the OM, HTPM, IMRPhenomD and TCTM models with respect to OM_3 (i.e., OM with $N_{\max} = 3$). We have found that in terms of the Bayes factor, at $t_0 = 0$, the IMRPhenomD is the preferred model, the second best ranked model being the TCTM_1 ; $\log_{10} \mathcal{B}_{\text{OM}_3}^{\text{IMRPhenomD}} \sim 8$ and $\log_{10} \mathcal{B}_{\text{TCTM}_1}^{\text{IMRPhenomD}} \sim 5$, showing a decisive (in the vocabulary of [112]) evidence towards the IMRPhenomD model. The preference for the nonlinear IMRPhenomD model remains consistent until $t_0/M \sim 15$, at which point the OM_2 exhibits a comparable evidence. It is also important to note that the nonlinear TCTM_1 model consistently offers superior fits to the data compared to the OM models at negative/early starting times. However, as anticipated, this difference also diminishes at late fitting starting times. Next, we have estimated the SNR required for observing confidently a tone amplitude for the OM models, with $N_{\max} = 1, 2, 3$. First, we have obtained that, at 90% credible level, the ratio of bias to statistical uncertainty $\epsilon/\sigma_e^{90\%}$ exceeds one for the models OM_1 and HTPM_1 when $\rho \sim 30$. This implies that analyses of the RD of upcoming loud GW events might be soon dominated by the systematic errors if those models are used. For the nonlinear and the $\text{OM}_{n \geq 2}$ models, we show that the systematic errors remain subdominant up to $\rho \sim 150$. Additionally, we observe that achieving a full observation and/or characterization of all the amplitude parameters of the linear models $\text{OM}_{n=2,3}$ would require a SNR $\rho \sim 30, 80$, respectively. However, the strong variability of their amplitudes pose reasonable doubts on the physical reliability of the models as compared to the full nonlinear solutions, which simply depend on the well-known progenitor parameters. Finally, we carried out parameter estimation with the same set of models on four additional waveforms from the SXS catalog, including one example from its Ext-CCE extension. We observe again the compelling preference for the nonlinear models compared to the OM and non-GR (HTPM) models regarding the evidence as well as (in the case of the IMRPhenomD model) the recovery bias, showing the robustness of the trends observed in our more detailed SXS:BBH:0305 analysis.

In summary, we have performed ringdown PE on five independent quasicircular NR simulations (not part of the calibration set of the IMR model considered) over a range of mass ratios and aligned, anti-aligned or vanishing spins. Our findings indicate that IMR-based nonlinear models such as the IMRPhenomD model, yield higher Bayes factors than the QNM-only models, especially in high-SNR ($\rho \approx 100$) scenarios. This implies a higher accuracy than QNM models in fitting NR ringdown waveforms up to early times. Moreover, the IMRPhenomD model results in tighter posterior distributions for the black hole final mass and spin. Additionally, we observe that the value of the evidence of the OM models saturates at $N_{\max} = 2$. The decrease of the evidence at $N_{\max} > 2$ could be induced by the expected nonlinearities affecting the early post-peak phase which, at the same time, may be causing the observed large instabilities on the amplitudes of the tones with $n > 1$ [64,65,67,121,122]. For our toy nonlinear model TCTM_1 , we observe similar posterior distributions than for the OM models, together with a better Bayes factor at early times—intermediate between that of OM models and that of the IMRPhenomD model. Tests with other NR calibrated models as the IMRPhenomPv2 and SEOBNRv4 approximants [20,123,124] provided the same qualitative results.

Hence, we conclude that the utilization of nonlinear models and, especially, well-established IMR models which are calibrated to the progenitor parameters, can be more pertinent when inferring physical parameters from a nonprecessing, quasicircular RD signal. This is particularly relevant when the analysis commences at the peak of the strain and is applicable to SNR ratios consistent with third-generation observatories such as ET and CE. Further investigation into other NR waveforms from different catalogs, specifically focusing on precessing binaries, will be performed elsewhere.

ACKNOWLEDGMENTS

This paper was initiated as a result of an internship carried out virtually under the Max Planck Institute for Gravitational Physics Hanover. We acknowledge the Max Planck Gesellschaft for support and we are grateful to the Atlas cluster computing team at MPG Hanover for their help. The authors are also thankful to Alex Nitz, Collin Capano, Sumit Kumar, and Yifan Wang for useful discussions, to Juan Calderon Bustillo, Gregorio Carullo, Will Farr and Vasco Gennari for helpful comments on the draft, and to an anonymous referee for insightful comments. P. M. and X. J. F. are supported by the Universitat de les Illes Balears (UIB); the Spanish Agencia Estatal de Investigación Grants No. PID2022-138626NB-I00, No. RED2022-134204-E, and No. RED2022-134411-T, funded by MCIN/AEI/10.13039/501100011033/FEDER, UE; the MCIN with funding from the European Union NextGenerationEU/PRTR (No. PRTR-C17.I1); the

Comunitat Autònoma de les Illes Balears through the Direcció General de Recerca, Innovació i Transformació Digital with funds from the Tourist Stay Tax Law (No. PDR2020/11-ITS2017-006), and the Conselleria d’Economia, Hisenda i Innovació Grant No. SINCO2022/6719. X. J. F. is also supported by the Spanish Ministerio de Ciencia, Innovación y Universidades (Beatriz Galindo, BG22-00034) and cofinanced by UIB.

APPENDIX A: ROBUSTNESS TESTS OF PRIOR CHOICES

In parameter estimation, the choice of prior range is always a crucial factor. In fact, even if the posterior distributions are rather similar, the Bayes evidence can

TABLE III. The table provides an overview of the priors used for all the models we consider in the paper. Note that we use a log-flat prior for A in TCTM as its order of magnitude is not known *a priori*; while all other parameters are uniformly distributed. Note that we use different priors for the amplitudes in different OM. The reasoning behind is that we observe broader, more loosely constrained posteriors in the higher overtones’ amplitudes, hence the prior ranges need to be extended accordingly. While for the remnant mass, a tighter choice of priors on higher overtone models will rule out the local minimum and thus represent a more physical analysis on OM.

Model	Parameter	Prior
OM ₀	Remnant mass	(0.5, 1.3)
	Remnant spin	(0, 0.99)
	Amplitudes	(0, 2)
	Phases	(0, 2 π)
OM _{1~2}	Remnant mass	(0.5, 1.3)
	Remnant spin	(0, 0.99)
	Amplitudes	(0, 10)
	Phases	(0, 2 π)
OM _{3~4}	Remnant mass	(0.5, 1.1)
	Remnant spin	(0, 0.99)
	Amplitudes	(0, 10)
	Phases	(0, 2 π)
TCTM _{n}	Remnant mass	(0.5, 1.3)
	Remnant spin	(0, 0.99)
	Amplitudes	(0, 2)
	Phases	(0, 2 π)
	$\log_{10} A$	(-5, 5)
	τ	(0, 100)
HTPM _{n}	Remnant mass	(0.5, 1.3)
	Remnant spin	(0, 0.99)
	Amplitudes	(0, 2)
	Phases	(0, 2 π)
	α	(-0.5, 1)
	β	(-0.5, 1)
IMRPhenomD	Mass ratio	(1, 8)
	Initial spin 1	(-0.99, 0.99)
	Initial spin 2	(-0.99, 0.99)
	Phases	(0, 2 π)

still be different for different prior assumptions. As shown in Table III, in our case, since we want to compare between the IMRPhenomD and OMs, the priors already differ in the first place that one is a IMR model that requires initial properties of the binary, while the another is only a RD model. For IMRPhenomD, the mass ratio of (1, 8) prior range +(-0.99, 0.99) spins priors would lead to a different prior range on the remnant mass after conversion. The new prior range is $\sim(0.85, 1)$ for the final mass, which is much different from the typical prior range we use for overtone model, i.e., (0.5, 1.3).

To examine the robustness of our tests on different prior assumptions, we also perform the same sampling for OM₂ with two new different priors on particularly the final mass. They are (0.7, 1.2) and (0.8, 1.1), respectively. In Fig. 7, the two new priors are denoted as “Prior2” and “Prior3” with the “Prior1” being (0.5, 1.3). In this plot, we show the $\log_{10} \mathcal{B}$ between IMRPhenomD and OM₂ for three different prior ranges and for five different waveforms. To examine the robustness of the choice of prior ranges, we compare the vertical three values in each column of the plot as they are computed on samplings of the same waveform. We find that the largest difference in the \log_{10} Bayes evidence we observe is in SXS:BBH:0305, which has a $\log_{10} \mathcal{B} \sim 1$ for

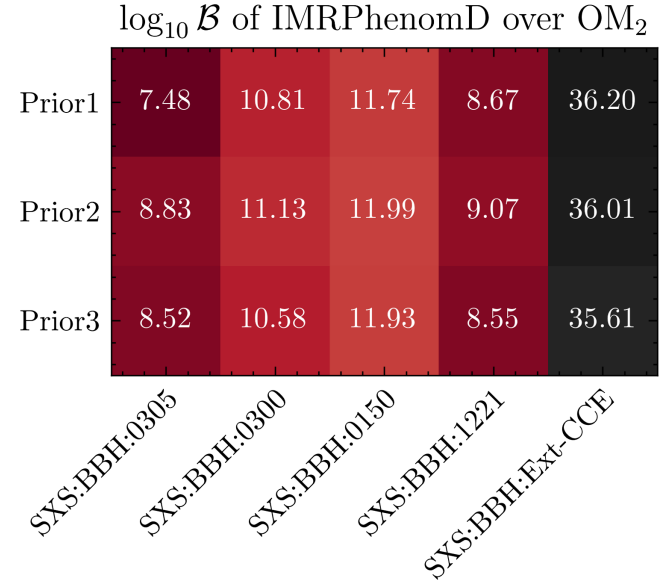


FIG. 7. We show the $\log_{10} \mathcal{B}$ between IMRPhenomD and OM₂ for 3 different prior ranges and for five different waveform. In this plot, the “Prior1”, “Prior2”, “Prior3” are used to denote different ranges for the final mass prior of, (0.5, 1.3), (0.7, 1.2), and (0.8, 1.1), respectively. To examine the robustness of the choice of prior ranges, we compare the vertical three values in each column of the plot as they are computed on samplings of different waveform. Comparing the values within a column and for the three columns of the plot, we do not observe significant differences. This suggests that the choices made on the priors, do not significantly influence the relative performance of the RD models.

one of the new prior sampling comparing to the typical prior sampling. However, this change is rather little compared to the absolute values of the Bayes factors, which have $\log_{10} \mathcal{B} > 7$ for all the priors. Moreover, we don't see any clear trend in the improvement/reduction of Bayes factors when the prior range shrinks, i.e., from "Prior1" to "Prior3". Therefore, the difference we observe are also possibly subject to the statistical errors of the samplings. Not to mention in other tests, the difference between the Bayes evidence are even smaller. Therefore, we conclude that the prior choice of our test is robust.

APPENDIX B: POSTERIOR OF Ext-CCE WAVEFORM

As another cross-check, we also present our bias analysis for the Cauchy characteristic Ext-CCE waveform from the additional SXS catalog particularly in terms of the mass/spin posterior distribution comparison of different models. The specific waveform we test is Ext-CCE:BBH:0002, which has true final dimensionless mass and spin m_f, a_f given as [0.946, 0.746].

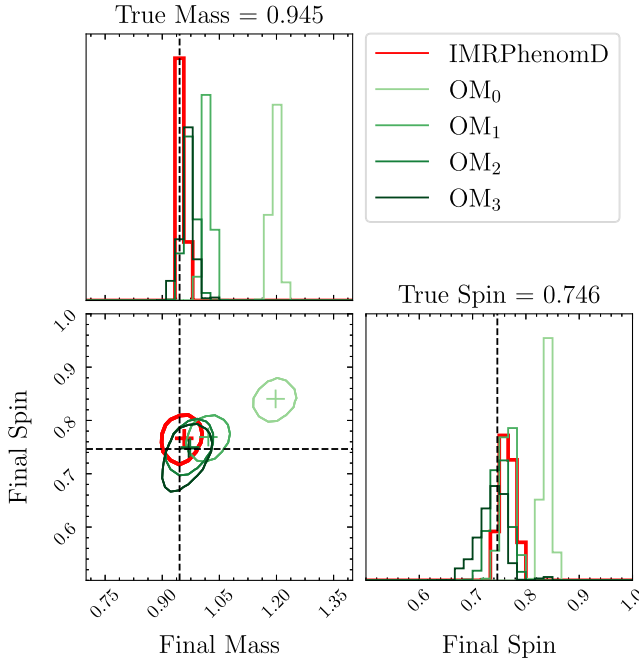


FIG. 8. We show the comparison of final mass and spin posterior distribution for the sampling of OM_{0-3} and IMRPhenomD for waveform Ext-CCE:BBH:0002 as a cross check. Each contour represents a 90% credible region on the mass-spin 2D plane for given model. The black dashed lines note the "true" final mass and spin. The "+" symbols denote the maximum likelihood values for each of the models considered. We assume the injection ρ to be 100 for all the cases, in order to see the clear comparison.

In Fig. 8, we show firstly the comparison of final mass and spin posterior distribution for the sampling of OM_{0-3} and IMRPhenomD. In the main text, we see that the posterior distributions improvement in successive OMs. Similarly, we also see here that the posterior distributions on the remnant mass and spin for OM improves significantly from OM_0 to OM_1 , but then converges at OM_3 . In particular, the epsilons values estimated for OM_2 and OM_3 are comparable, as the maximum likelihood values for both models almost overlap. The IMRPhenomD model here also shows a comparable parameter estimation performance to the $OM_{2,3}$ models. IMRPhenomD gives a more faithful recovery for the final mass, while it performs slightly worse in terms of the final spin as we can see from the 1D marginalized distribution. Therefore, the results obtained for the Ext-CCE:BBH:0002 waveform is consistent with the results obtained for SXS:BBH:0305 presented in the main text.

In Fig. 9, we show then the comparison of final mass and spin posterior distribution for the sampling of OM_2 , TCTM₁, HTPM₁ and IMRPhenomD assuming $\rho = 100$. Again, this is test about different types of models. We can see from the 90% credible contours that the nonlinear

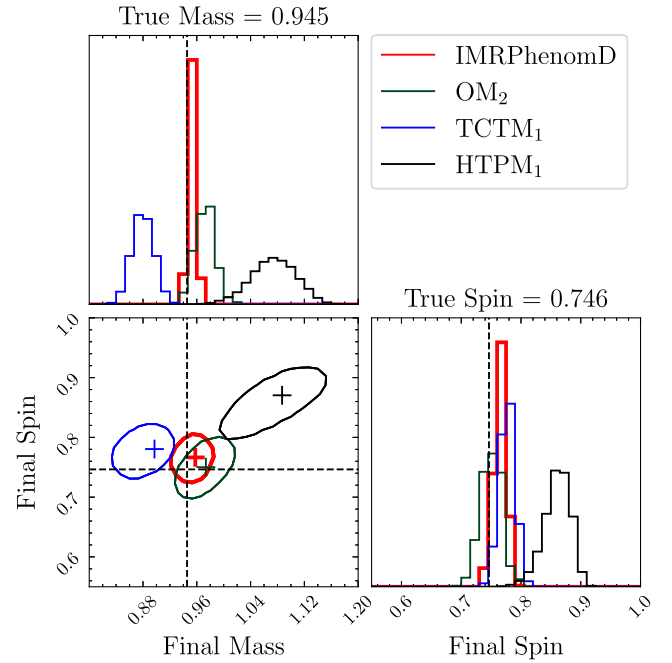


FIG. 9. We show the comparison of final mass and spin posterior distribution for the sampling of OM_2 , TCTM₁, HTPM₁ and IMRPhenomD for waveform Ext-CCE:BBH:0002. Each contour represents a 90% credible region on the mass-spin 2D plane for given model. The "+" symbols denote the maximum likelihood values for each of the models considered here. The black dashed lines note the "true" final mass and spin.

IMRPhenomD model performs the best in both the recovery accuracy and precision with only four free parameters. While for all the other models we have eight parameters. Unlike the conclusion in the main text, here the other nonlinear model TCTM₁ has much worse

posterior distributions comparing to the corresponding OM₂ (i.e., having the same number of parameters). The model with the worst performance here is still HTPM₁ as it considers the deviation to GR, which leads then to a looser/biased constraint on the remnant mass and spin.

-
- [1] B. P. Abbott *et al.* (The LIGO Scientific and the Virgo Collaborations), *Phys. Rev. Lett.* **116**, 061102 (2016).
 - [2] B. P. Abbott *et al.* (The LIGO Scientific and the Virgo Collaborations), *Phys. Rev. X* **9**, 031040 (2019).
 - [3] T. Venumadhav, B. Zackay, J. Roulet, L. Dai, and M. Zaldarriaga, *Phys. Rev. D* **101**, 083030 (2020).
 - [4] R. Abbott *et al.* (The LIGO Scientific and the Virgo Collaborations), *Phys. Rev. X* **11**, 021053 (2021).
 - [5] R. Abbott *et al.* (The LIGO Scientific and the Virgo Collaborations), *Phys. Rev. D* **109**, 022001 (2024).
 - [6] R. Abbott *et al.* (The LIGO Scientific, the Virgo, and the KAGRA Collaborations), *Phys. Rev. X* **13**, 041039 (2023).
 - [7] A. H. Nitz, S. Kumar, Y.-F. Wang, S. Kasta, S. Wu, M. Schäfer, R. Dhurkunde, and C. D. Capano, *Astrophys. J.* **946**, 59 (2023).
 - [8] J. Aasi *et al.* (The LIGO Scientific Collaboration), *Classical Quantum Gravity* **32**, 074001 (2015).
 - [9] F. Acernese *et al.* (The Virgo Collaboration), *Classical Quantum Gravity* **32**, 024001 (2015).
 - [10] Y. Aso, Y. Michimura, K. Somiya, M. Ando, O. Miyakawa, T. Sekiguchi, D. Tatsumi, and H. Yamamoto (The KAGRA Collaboration), *Phys. Rev. D* **88**, 043007 (2013).
 - [11] B. P. Abbott *et al.* (The LIGO Scientific and the Virgo Collaborations), *Phys. Rev. Lett.* **116**, 221101 (2016); **121**, 129902(E) (2018).
 - [12] B. P. Abbott *et al.* (The LIGO Scientific and the Virgo Collaborations), *Phys. Rev. D* **100**, 104036 (2019).
 - [13] R. Abbott *et al.* (The LIGO Scientific and the Virgo Collaborations), *Phys. Rev. D* **103**, 122002 (2021).
 - [14] R. Abbott *et al.* (The LIGO Scientific, the Virgo, and the KAGRA Collaborations), [arXiv:2112.06861](https://arxiv.org/abs/2112.06861).
 - [15] B. P. Abbott *et al.* (The KAGRA, the LIGO Scientific, and the Virgo Collaborations), *Living Rev. Relativity* **21**, 3 (2018).
 - [16] G. Pratten *et al.*, *Phys. Rev. D* **103**, 104056 (2021).
 - [17] S. Ossokine *et al.*, *Phys. Rev. D* **102**, 044055 (2020).
 - [18] A. Nagar, P. Rettengo, R. Gamba, S. Albanesi, A. Albertini, and S. Bernuzzi, *Phys. Rev. D* **108**, 124018 (2023).
 - [19] C. García-Quirós, M. Colleoni, S. Husa, H. Estellés, G. Pratten, A. Ramos-Buades, M. Mateu-Lucena, and R. Jaume, *Phys. Rev. D* **102**, 064002 (2020).
 - [20] A. Bohé *et al.*, *Phys. Rev. D* **95**, 044028 (2017).
 - [21] R. Cotesta, A. Buonanno, A. Bohé, A. Taracchini, I. Hinder, and S. Ossokine, *Phys. Rev. D* **98**, 084028 (2018).
 - [22] V. Varma, S. E. Field, M. A. Scheel, J. Blackman, D. Gerosa, L. C. Stein, L. E. Kidder, and H. P. Pfeiffer, *Phys. Rev. Res.* **1**, 033015 (2019).
 - [23] E. W. Leaver, *Proc. R. Soc. A* **402**, 285 (1985).
 - [24] S. L. Detweiler, *Astrophys. J.* **239**, 292 (1980).
 - [25] K. D. Kokkotas and B. G. Schmidt, *Living Rev. Relativity* **2**, 2 (1999).
 - [26] W. H. Press and S. A. Teukolsky, *Astrophys. J.* **185**, 649 (1973).
 - [27] S. A. Teukolsky, *Astrophys. J.* **185**, 635 (1973).
 - [28] S. W. Hawking, *Commun. Math. Phys.* **25**, 152 (1972).
 - [29] B. Carter, *Phys. Rev. Lett.* **26**, 331 (1971).
 - [30] D. C. Robinson, *Phys. Rev. Lett.* **34**, 905 (1975).
 - [31] E. Berti, V. Cardoso, and M. Casals, *Phys. Rev. D* **73**, 024013 (2006).
 - [32] X. Jiménez Forteza, S. Bhagwat, P. Pani, and V. Ferrari, *Phys. Rev. D* **102**, 044053 (2020).
 - [33] X. J. Forteza, S. Bhagwat, S. Kumar, and P. Pani, *Phys. Rev. Lett.* **130**, 021001 (2023).
 - [34] I. Kamaretsos, M. Hannam, S. Husa, and B. S. Sathyaprakash, *Phys. Rev. D* **85**, 024018 (2012).
 - [35] I. Kamaretsos, M. Hannam, and B. Sathyaprakash, *Phys. Rev. Lett.* **109**, 141102 (2012).
 - [36] L. London, D. Shoemaker, and J. Healy, *Phys. Rev. D* **90**, 124032 (2014); **94**, 069902(E) (2016).
 - [37] L. T. London, *Phys. Rev. D* **102**, 084052 (2020).
 - [38] S. A. Hughes and K. Menou, *Astrophys. J.* **623**, 689 (2005).
 - [39] O. Dreyer, B. J. Kelly, B. Krishnan, L. S. Finn, D. Garrison, and R. Lopez-Aleman, *Classical Quantum Gravity* **21**, 787 (2004).
 - [40] V. Gennari, G. Carullo, and W. Del Pozzo, [arXiv:2312.12515](https://arxiv.org/abs/2312.12515).
 - [41] M. Isi, M. Giesler, W. M. Farr, M. A. Scheel, and S. A. Teukolsky, *Phys. Rev. Lett.* **123**, 111102 (2019).
 - [42] G. Carullo, W. Del Pozzo, and J. Veitch, *Phys. Rev. D* **99**, 123029 (2019); **100**, 089903(E) (2019).
 - [43] J. Calderón Bustillo, P. D. Lasky, and E. Thrane, *Phys. Rev. D* **103**, 024041 (2021).
 - [44] M. Isi and W. M. Farr, [arXiv:2202.02941](https://arxiv.org/abs/2202.02941).
 - [45] E. Finch and C. J. Moore, *Phys. Rev. D* **106**, 043005 (2022).
 - [46] R. Cotesta, G. Carullo, E. Berti, and V. Cardoso, *Phys. Rev. Lett.* **129**, 111102 (2022).
 - [47] S. Ma, L. Sun, and Y. Chen, *Phys. Rev. D* **107**, 084010 (2023).
 - [48] M. Isi and W. M. Farr, *Phys. Rev. Lett.* **131**, 169001 (2023).
 - [49] G. Carullo, R. Cotesta, E. Berti, and V. Cardoso, *Phys. Rev. Lett.* **131**, 169002 (2023).
 - [50] Y.-F. Wang, C. D. Capano, J. Abedi, S. Kasta, B. Krishnan, A. B. Nielsen, A. H. Nitz, and J. Westerweck, [arXiv:2310.19645](https://arxiv.org/abs/2310.19645).

- [51] R. Abbott *et al.* (The LIGO Scientific and the Virgo Collaborations), *Phys. Rev. Lett.* **125**, 101102 (2020).
- [52] R. Abbott *et al.* (The LIGO Scientific and the Virgo Collaborations), *Astrophys. J. Lett.* **900**, L13 (2020).
- [53] C. D. Capano, M. Cabero, J. Westerweck, J. Abedi, S. Kastha, A. H. Nitz, A. B. Nielsen, and B. Krishnan, *Phys. Rev. Lett.* **131**, 221402 (2023).
- [54] C. D. Capano, J. Abedi, S. Kastha, A. H. Nitz, J. Westerweck, Y.-F. Wang, M. Cabero, A. B. Nielsen, and B. Krishnan, [arXiv:2209.00640](https://arxiv.org/abs/2209.00640).
- [55] H. Siegel, M. Isi, and W. M. Farr, *Phys. Rev. D* **108**, 064008 (2023).
- [56] S. Gossan, J. Veitch, and B. S. Sathyaprakash, *Phys. Rev. D* **85**, 124056 (2012).
- [57] R. Brito, A. Buonanno, and V. Raymond, *Phys. Rev. D* **98**, 084038 (2018).
- [58] G. Carullo, L. van der Schaaf, L. London, P. T. H. Pang, K. W. Tsang, O. A. Hannuksela, J. Meidam, M. Agathos, A. Samajdar, A. Ghosh, T. G. F. Li, W. Del Pozzo, and C. Van Den Broeck, *Phys. Rev. D* **98**, 104020 (2018).
- [59] Asharp Strain Sensitivity, <https://dcc.ligo.org/LIGO-T2300041/public> (2023) (accessed: 27-01-2023).
- [60] M. Maggiore *et al.*, *J. Cosmol. Astropart. Phys.* **03** (2020) 050.
- [61] M. Evans *et al.*, [arXiv:2109.09882](https://arxiv.org/abs/2109.09882).
- [62] LISA Science Study Team and ESA Study Team *et al.*, [arXiv:2402.07571](https://arxiv.org/abs/2402.07571).
- [63] S. Bhagwat, D. A. Brown, and S. W. Ballmer, *Phys. Rev. D* **94**, 084024 (2016); **95**, 069906(E) (2017).
- [64] V. Baibhav, M. H.-Y. Cheung, E. Berti, V. Cardoso, G. Carullo, R. Cotesta, W. Del Pozzo, and F. Duque, *Phys. Rev. D* **108**, 104020 (2023).
- [65] S. Bhagwat, X. J. Forteza, P. Pani, and V. Ferrari, *Phys. Rev. D* **101**, 044033 (2020).
- [66] M. Giesler, M. Isi, M. A. Scheel, and S. A. Teukolsky, *Phys. Rev. X* **9**, 041060 (2019).
- [67] X. J. Forteza and P. Mourier, *Phys. Rev. D* **104**, 124072 (2021).
- [68] M. H.-Y. Cheung *et al.*, *Phys. Rev. Lett.* **130**, 081401 (2023).
- [69] K. Takahashi and H. Motohashi, [arXiv:2311.12762](https://arxiv.org/abs/2311.12762).
- [70] M. Okounkova, [arXiv:2004.00671](https://arxiv.org/abs/2004.00671).
- [71] J. L. Ripley, N. Loutrel, E. Giorgi, and F. Pretorius, *Phys. Rev. D* **103**, 104018 (2021).
- [72] P. Mourier, X. Jiménez Forteza, D. Pook-Kolb, B. Krishnan, and E. Schnetter, *Phys. Rev. D* **103**, 044054 (2021).
- [73] S. R. Green, S. Hollands, L. Sberna, V. Toomani, and P. Zimmerman, *Phys. Rev. D* **107**, 064030 (2023).
- [74] L. London, [arXiv:2312.17678](https://arxiv.org/abs/2312.17678).
- [75] E. W. Leaver, *Phys. Rev. D* **34**, 384 (1986).
- [76] H.-P. Nollert, *Classical Quantum Gravity* **16**, R159 (1999).
- [77] M. Ansorg and R. Panosso Macedo, *Phys. Rev. D* **93**, 124016 (2016).
- [78] K. Mitman *et al.*, *Phys. Rev. Lett.* **130**, 081402 (2023).
- [79] N. Khera, A. Ribes Metidieri, B. Bonga, X. J. Forteza, B. Krishnan, E. Poisson, D. Pook-Kolb, E. Schnetter, and H. Yang, *Phys. Rev. Lett.* **131**, 231401 (2023).
- [80] M. Boyle *et al.*, *Classical Quantum Gravity* **36**, 195006 (2019).
- [81] S. A. Teukolsky, *Phys. Rev. Lett.* **29**, 1114 (1972).
- [82] E. Berti, V. Cardoso, and A. O. Starinets, *Classical Quantum Gravity* **26**, 163001 (2009).
- [83] E. Finch and C. J. Moore, *Phys. Rev. D* **103**, 084048 (2021).
- [84] A. Dhani and B. S. Sathyaprakash, [arXiv:2107.14195](https://arxiv.org/abs/2107.14195).
- [85] E. Berti, <https://pages.jh.edu/eberti2/ringdown/>.
- [86] E. Berti, V. Cardoso, and C. M. Will, *Phys. Rev. D* **73**, 064030 (2006).
- [87] G. B. Cook, Kerr quasinormal modes: $s = -2$, $n = 0-7$ (version 1), Zenodo, [10.5281/zenodo.2650358](https://zenodo.org/record/2650358) (2019).
- [88] G. B. Cook and M. Zalutskiy, *Phys. Rev. D* **90**, 124021 (2014).
- [89] L. C. Stein, *J. Open Source Software* **4**, 1683 (2019).
- [90] A. K.-W. Chung, P. Wagle, and N. Yunes, *Phys. Rev. D* **107**, 124032 (2023).
- [91] A. K.-W. Chung, P. Wagle, and N. Yunes, [arXiv:2312.08435](https://arxiv.org/abs/2312.08435).
- [92] P. Mourier and X. Jiménez Forteza, https://codeberg.org/GW_Ringdown.
- [93] X. Jiménez Forteza and P. Mourier, https://github.com/frcojimenez/GW_Rdown.
- [94] V. Cardoso, <https://centra.tecnico.ulisboa.pt/network/grit/files/ringdown/>.
- [95] G. B. Cook, *Phys. Rev. D* **102**, 024027 (2020).
- [96] K. Mitman *et al.*, *Phys. Rev. D* **106**, 084029 (2022).
- [97] M. Giesler, M. Isi, M. A. Scheel, and S. A. Teukolsky, *Phys. Rev. X* **9**, 041060 (2019).
- [98] S. Bhagwat, M. Okounkova, S. W. Ballmer, D. A. Brown, M. Giesler, M. A. Scheel, and S. A. Teukolsky, *Phys. Rev. D* **97**, 104065 (2018).
- [99] X. Jiménez Forteza, S. Bhagwat, P. Pani, and V. Ferrari, *Phys. Rev. D* **102**, 044053 (2020).
- [100] G. Carullo *et al.*, *Phys. Rev. D* **98**, 104020 (2018).
- [101] R. H. Price, *Phys. Rev. D* **5**, 2439 (1972).
- [102] G. Carullo and M. De Amicis, [arXiv:2310.12968](https://arxiv.org/abs/2310.12968).
- [103] P. Papadopoulos and J. A. Font, *Phys. Rev. D* **63**, 044016 (2001).
- [104] L. Sberna, P. Bosch, W. E. East, S. R. Green, and L. Lehner, *Phys. Rev. D* **105**, 064046 (2022).
- [105] J. Redondo-Yuste, D. Pereñíguez, and V. Cardoso, *Phys. Rev. D* **109**, 044048 (2024).
- [106] D. Sharma, P. Mourier, X. Jiménez Forteza, D. Pook-Kolb, B. Krishnan, and J. Jaramillo (to be published).
- [107] S. Khan, S. Husa, M. Hannam, F. Ohme, M. Pürrer, X. Jiménez Forteza, and A. Bohé, *Phys. Rev. D* **93**, 044007 (2016).
- [108] J. E. Thompson, E. Hamilton, L. London, S. Ghosh, P. Kolitsidou, C. Hoy, and M. Hannam, [arXiv:2312.10025](https://arxiv.org/abs/2312.10025).
- [109] A. Nitz *et al.*, gwastro/pycbc: v2.2.1 release of pycbc (2023).
- [110] X. Jiménez-Forteza, D. Keitel, S. Husa, M. Hannam, S. Khan, and M. Pürrer, *Phys. Rev. D* **95**, 064024 (2017).
- [111] F. Hofmann, E. Barausse, and L. Rezzolla, *Astrophys. J.* **825**, L19 (2016).
- [112] R. E. Kass and A. E. Raftery, *J. Am. Stat. Assoc.* **90**, 773 (1995).
- [113] D. A. B. Iozzo *et al.*, *Phys. Rev. D* **103**, 124029 (2021).

- [114] A. Ashtekar and B. Krishnan, *Living Rev. Relativity* **7**, 10 (2004).
- [115] J. Skilling, *Bayesian Anal.* **1**, 833 (2006).
- [116] E. Maggio, H. O. Silva, A. Buonanno, and A. Ghosh, *Phys. Rev. D* **108**, 024043 (2023).
- [117] M. Cabero, J. Westerweck, C. D. Capano, S. Kumar, A. B. Nielsen, and B. Krishnan, *Phys. Rev. D* **101**, 064044 (2020).
- [118] J. S. Speagle, *Mon. Not. R. Astron. Soc.* **493**, 3132 (2020).
- [119] M. Lagos and L. Hui, *Phys. Rev. D* **107**, 044040 (2023).
- [120] M. Ho-Yeuk Cheung, E. Berti, V. Baibhav, and R. Cotesta, [arXiv:2310.04489](https://arxiv.org/abs/2310.04489).
- [121] M. H.-Y. Cheung, E. Berti, V. Baibhav, and R. Cotesta, [arXiv:2310.04489](https://arxiv.org/abs/2310.04489).
- [122] H. Zhu, J. L. Ripley, A. Cárdenas-Avendaño, and F. Pretorius, *Phys. Rev. D* **109**, 044010 (2024).
- [123] M. Hannam, P. Schmidt, A. Bohé, L. Haegel, S. Husa, F. Ohme, G. Pratten, and M. Pürrer, *Phys. Rev. Lett.* **113**, 151101 (2014).
- [124] A. Bohé, M. Hannam, S. Husa, F. Ohme, M. Pürrer, and P. Schmidt (LIGO Scientific and Virgo Collaborations), PhenomPv2—technical notes for the LAL implementation, Technical Report, LIGO-T1500602, 2016.